Critical Role of Water on the Synthesis and Gelling of γ-In 2 S 3 Nanoribbons with a Giant Aspect Ratio

Lilian Guillemeney, Laurent Lermusiaux, Patrick Davidson, Austin Hubley, Stefano Pierini, Debora Pierucci, Gilles Patriarche, Bruno Canut, Emmanuel Lhuillier, Benoît Mahler, et al.

To cite this version:

Lilian Guillemeney, Laurent Lermusiaux, Patrick Davidson, Austin Hubley, Stefano Pierini, et al.. Critical Role of Water on the Synthesis and Gelling of γ-In 2 S 3 Nanoribbons with a Giant Aspect Ratio. Chemistry of Materials, 2022, 34 (20), pp.9270-9281. 10.1021/acs.chemmater.2c02623 . hal-03861768

HAL Id: hal-03861768
https://hal.science/hal-03861768v1

Submitted on 21 Nov 2022

Critical role of water on the synthesis and gelling of γ-In_2S_3 nanoribbons with giant aspect ratio

Lilian Guillemeney,[†] Laurent Lermusiaux,[†] Patrick Davidson,[‡] Austin Hubley,[†] Stefano Pierini,[¶] Debora Pierucci,[§] Gilles Patriarche,[§] Bruno Canut,[‖] Emmanuel Lhuillier,[¶] Benoît Mahler,[⊥] and Benjamin Abécassis[*,†]

†ENSL, CNRS, Laboratoire de Chimie UMR 5182, 46 allée d'Italie, 69364 Lyon France

‡Laboratoire de Physique des Solides, Université Paris-Saclay, CNRS, 91405 Orsay

¶Sorbonne Université, CNRS, Institut des NanoSciences de Paris, INSP, F-75005 Paris, France

§Centre de Nanosciences et de Nanotechnologies, CNRS, Université Paris Saclay, 91120 Palaiseau, France

‖Univ. Lyon, CNRS, ECL, UCBL, INSA Lyon, CPE, INL UMR5270, F-69621 Villeurbanne, France.

⊥Univ. Lyon, Université Claude Bernard Lyon 1, CNRS, Institut Lumiere Matière (iLM), F-69622 Villeurbanne, France

E-mail: benjamin.abecassis@ens-lyon.fr

Abstract

We report the synthesis of ultrathin indium sulfide In_2S_3 nanoribbons which display a giant aspect ratio using a simple and fast solvothermal method. They have a sub-nanometer thickness controlled at the atomic level, a width of (8.7 ± 0.1) nm and a length which can reach several micrometers. We determine the atomic composition of the inorganic core by Rutherford backscattering spectrometry (RBS) and measure by X-ray photoelectron spectrometry (XPS) an oleylamine surface coverage of 2.3 ligands per nm^2. X-ray diffraction experiments and simulations as well as high-resolution dark-field STEM point toward a $P\bar{3}m1$ trigonal crystallographic structure (γ phase). Transport measurements show that the nanoribbons display n-type semiconductor unipolar behavior. Their lateral dimensions can be tuned by reaction time, temperature and by the amount of water present in the reaction medium: anhydrous synthesis conditions lead to hexagonal nanoplates, whereas controlled addition of water induces a symmetry break yielding long rectangular nanoribbons. Depending on the dispersion solvent, these long ribbon-like nanoparticles can form either well-dispersed colloids or bundles in which they stack face-to-face. Their large aspect ratio induces the formation of gels at volume fractions as low as 1.3×10^{-4} making them supergelators. The kinetics of gelation is strongly accelerated by an increase in the relative humidity of the ambient atmosphere.

Introduction

Colloidal nanoplatelets are ultrathin 2D nanomaterials whose outstanding optical properties triggered a wide research effort.[1] However they usually contain heavy metals such as cadmium,[2,3] lead[4] or mercury whose toxicity is a drawback to their wide acceptance. In the quest for more environmentally and health benign materials, indium based nanoparticles are often thought of as possible alternatives. Among them, indium sulfide is a wide band gap semiconductor material which has useful properties such as long-term stability and low toxicity when compared to its toxic counterparts. With band gaps ranging from 1.65 eV to 3.7 eV depending on the crystal phase reported in the literature,[5,6] In_2S_3 could be used in a variety of optoelectronic applications such as buffer layers in photovoltaics,[7] in display devices and photodetectors,[8–12] or for water splitting.[13] Although research on indium sulfide colloidal nanoparticles has been quite active in the past years, notably in the exploration of different synthetic pathways, only partial shape control has been achieved to date. For example, several reports describe the synthesis of 1D nanomaterials such as long nanotubes[14] using $InCl_3$ and sulfur in oleylamine, while di-tert-butyl disulfide and indium acetylacetonate in oleylamine yield β-In_2S_3 nanorods with a mean length of 170 nm.[15] As far as 2D nanomaterials are concerned, Park *et al.* have first reported the colloidal synthesis of In_2S_3 hexagonal nanoplates[8] while the Pradhan group obtained large (>1 μm) indium sulfide nanosheets through the thermal decomposition of indium tris-diethyldithiocarbamate in hexadecylamine.[16] Similar wrinkled nanosheets have been observed as transient intermediates towards smaller ($\simeq$ 60 nm) hexagonal In_2S_3 nanoplates when $InCl_3$ and thiourea are used as precursors in oleylamine.[17] Shape control can also be achieved using other strategies without varying the precursor sources: Ni *et al.* obtained nanotubes from the self-assembly of ultrathin nanocoils synthesized from indium acetate and sulfur in octylamine,[18,19] whereas Tian *et al.* showed that nanoflakes, spherical nanoparticles or nanobelts could be obtained with the introduction of an appropriate metallic ion in the initial mixture.[20] Finally, starting from the same type of precursors, other materials with different indium oxidation states can be obtained. For instance, InS materials may appear in four different allotropic varieties (orthorhombic, monoclinic, cubic and tetragonal) with the orthorhombic *Pnnm* structure predicted to be the most stable.[21] 1D-InS nanomaterials have already been reported in the form of wires or rods,[22] whereas 2D-InS nanomaterials were obtained from a solvothermal synthesis between thioacetamide and indium metal resulting in the formation of thin NR.[23] Overall, the control of particle shape and atomic composition in indium sulfide nanoparticles is strongly dependent on the synthesis parameters. More specifically, the aspect ratios for 2D materials cannot be controlled with current synthetic strategies and either relatively small (below 100 nm) or very large (>1 μm) square shaped platelets can be synthesized.

Phase identification for indium sulfide has thus far remained ambiguous. Most reported syntheses are thought to yield In_2S_3, but definitive attribution of the crystal structure is often difficult because the X-ray diffraction patterns do not match exactly the entries of crystallographic databases. These discrepancies have been attributed to the anisotropy of the nanoparticles, since reflections corresponding to small crystalline domains are expected to be broadened according to Scherrer's equation.[24] In the case of subnanometer dimensions, this broadening can be so significant that these peaks may be experimentally difficult to observe. In the Powder Diffraction Files of the International Centre for Diffraction Data (ICDD), four different In_2S_3 phases are reported. The cubic phase corresponding to the space group $Fd\overline{3}m$ (n°227) is often coined the α phase, while the most common is the tetragonal β phase bearing the $I4_1/amd$ (n°141) space group. Two other phases with a trigonal crystal system have also been reported, one with a rhombohedral space group ($R\overline{3}c$, ϵ phase) and the other with a hexagonal space group ($P\overline{3}m1$, γ phase). Pistor *et al.* describe three different structures of In_2S_3[25] : a low-temperature tetragonal phase β, an intermediate-temperature cubic phase α and a high-temperature trigonal phase γ, also reported by Diehl *et al.*[26] In any case, the experimental distinction between tetragonal β and cubic α phases is difficult to make without high-quality X-ray diffraction data. We point out that ambiguities exist in the designation of the different In_2S_3 phases.[25] First, the low-temperature cubic phase was initially coined α while the higher-temperature tetragonal phase was called β.[25] Later, it was shown that the initial report misidentified the low-temperature phase as being cubic. In fact, this low-temperature phase is tetragonal and a transition towards the cubic structure is observed as temperature increases. Hence, some authors have renamed the cubic phase β so that the names of the different phases will be consistent and follow the right alphabetical order as temperature increases. However, this has created much ambiguity. For instance, the cubic phase is named α in some files of the international crystallographic database and this notation is also present in publications. Second, several reports use the notation γ[17,27,28] when reporting the ϵ phase[29] (JCPDS 33-0624). In this contribution, we will abide by the notations of Pistor *et al.*[25] and designate the different phases as described above.

Nanoparticles can assemble into a wide range of structures at a larger scale. Among them, gels are defined as low volume-fraction dispersions (typically between 0.1% and 10% in volume) with solid-like rheological properties arising from the self-assembled percolating network made by their components. They can be made of small organic molecules which form threaded structures, polymers or colloidal particles with attractive interactions. In this case, a network of particles without long-range order percolates through the whole solution and induces the gelation. Gels are classically observed in dispersions of large micron-sized particles, but the formation of gels from nanoparticles has also raised significant interest. In this case, nanoparticle gels can be subsequently dried to form aerogels whose porosity and large surface area are highly beneficial for various applications such as photocatalysis or sensing.[30] Current strategies to make gels from nanoparticles involve tuning the interaction potential between small isotropic building blocks.[31,32] As the interaction shifts from repulsive to attractive depending on various factors such as solvent, temperature, or concentration in depletant, the colloidal dispersion is destabilized and eventually forms a gel. Both thermodynamic and kinetic effects must be taken into account to rationalize the gelling behavior of colloidal dispersions of nanoparticles.[33] Overly fast destabilization triggered by a large interaction strength leads to irreversible aggregation and precipitation, while with softer interaction, slower aggregation kinetics enables the particle network to span the whole solution. Another parameter to consider is the aspect ratio of the particles since highly anisotropic particles will more easily form percolating structures than spherical ones.

Here, we present the solvothermal synthesis of ultrathin γ-$\mathrm{In_2S_3}$ NR with a high aspect ratio. Using multiple techniques, we ascribe the NR composition and crystallographic structure to trigonal $P\overline{3}m1$ γ-$\mathrm{In_2S_3}$. We find that water added during the synthesis induces anisotropic growth, yielding long NR which reach more than one micrometer in length. We study their solvent-dependent organization in solution using small angle X-ray scattering and show that they tend to form bundles and to precipitate in toluene, whereas unbundled NR are obtained on short time scales when using tetrahydrofuran. In some instances, we discover that gels form due to the high anisotropy of the NR. The kinetics of the gelling then depends on the water content of the ambient atmosphere.

Experimental Section

Chemicals

Indium (III) chloride (anhydrous, 99+%) and THF (HPLC grade, 99.7%) were purchased from Fisher-Alfa Aesar. Indium (III) chloride was stored and manipulated in an oxygen and water-free glovebox. Sulfur (powder, 99.998%) was purchased from Sigma-Aldrich. Oleylamine (approximate C18-content 80-90%) was purchased from Fisher-Acros Organics. Absolute ethanol and toluene ($\geq$ 99.5%) were purchased from VWR.

Solvothermal Synthesis of In_2S_3 NR

Unless otherwise stated all experiment except the weighing of $InCl_3$ are performed in air. The long ultrathin nanoribbons presented in the main text are obtained as follows. 0.2654 g of anhydrous indium (III) chloride (1.2 mmol, 1 eq.), 0.0577 g of sulfur powder (1.8 mmol, 1.5 eq.), 11.8 mL of oleylamine, 170 μL of water (9.6 mmol, 8 eq.) are introduced in a 20 mL Teflon-lined autoclave. The reaction mixture is sonicated for 10 minutes with an ultrasonic probe to obtain a homogeneous solution. The autoclave is then sealed and heated in an oven at 215°C for 2 h under agitation. Once cooled down to room temperature, the resulting yellow viscous mixture is centrifuged for 5 minutes at 6153g; the product is then redispersed in 5 mL of ethanol before being centrifuged for 5 minutes at 6153g. The product is then redispersed in 5 mL of toluene and 3 mL of absolute ethanol are added. The solution is centrifuged again for 5 minutes at 6153g, and this last step is repeated at least once with a redispersion in 5 mL of toluene. The final yellow product is redispersed in 10 mL of toluene. The typical mass concentration in NR obtained at the end of the purification process is 31 g/L.

Rutherford Backscattering Spectrometry

The sample, initially in powder form, was deposited on a carbon adhesive tape. The analysis was performed with $^4He^+$ ions of 2 MeV energy delivered by the 4 MV Van de Graaff accelerator of the "ANAFIRE" platform (Institut de Physique des 2 Infinis, Lyon). The backscattered particles were detected with a 15 keV resolution implanted junction set at an angle of 169° with respect to the beam axis. The experimental data were fitted with the help of the SIMNRA simulation code (http://www2.if.usp.br/lamfi/guia-simnra.pdf).

X-ray Photoelectron Spectroscopy

XPS spectra were recorded on a THERMO K-alpha+ spectrometer with the Al Kα line used as the excitation source at the Laboratoire Science et Surface of Ecully (Serma Technologies).

Transmission Electron Microscopy and High-resolution Electron Microscopy

TEM images were acquired on a JEOL JEM-1400 (accelerating voltage of 120 kV). The samples were prepared by drop-casting In_2S_3 NR suspensions in toluene onto 200 mesh carbon-coated copper grids. To avoid agglomeration on the TEM grids, the suspension was diluted a minima by a factor of ten and sonicated 2 minutes in an ultrasonic bath just before deposition. High-angle annular dark-field scanning transmission electron microscopy (HAADF-STEM) pictures have been acquired using a JEOL JEM-ARM200F Cold FEG NeoARM operating at 200 kV.

X-ray Diffraction Experiments

Powder X-Ray Diffraction (XRD) analyses were performed with a PANalytical Empyrean X-ray diffractometer equipped with a 1.8 kW Cu Kα ceramic tube, operating at 45 kV and 40 mA and a PIXcel3D 2x2 area detector.

Simulation of X-ray Powder Diffraction

Atomic models of In_2S_3 nanoribbons were generated using the Crystal Maker software as follows: a new crystal was created and the corresponding space group, lattice parameters and atomic positions in the unit cell were entered following Pistor *et al.*[25] The unit cell was expanded along the principal crystallographic directions with ratios 1×10×100. The structure was then exported as an xyz coordinate text file which serves as input for calculation of the X-ray diffractogram using the Debyer program (https://github.com/wojdyr/debyer) which calculates the scattering pattern from atomic coordinates using Debye's scattering equation.

Small Angle X-ray Scattering

Synchrotron SAXS experiments were performed on the SWING beamline at the SOLEIL synchrotron (Saint-Aubin, France) using a X-ray energy of 16 keV with a sample-to-detector distance of 1 m. The 2D scattering patterns were radially averaged using beamline-specific procedures. The I(q) data were fitted using SasView (http://www.sasview.org/).

UV-visible Spectroscopy

UV-vis absorption spectra were measured on Lambda 750 Perkin-Elmer and Jasco V-770 spectrophotometers. For the measurements, NR were dispersed in THF (0.027 $g.L^{-1}$) in 1 cm thick quartz cuvettes (Hellma).

Raman Spectroscopy

Measurements were conducted at room temperature using a commercial confocal HORIBA LabRam HR Evolution micro-Raman microscope with a 100× objective and a 532 nm laser excitation. Spectra were recorded between 50 cm^{-1} and 500 cm^{-1} with 1800 lines/mm grating resulting in a resolution of 1 cm^{-1}. Spectrometer calibration was set using the 520.5 cm^{-1} band of a Si crystal. The effective laser power at the exit of the objective was approximately 0.25 mW.

Electrodes for Contact Pads

A Si/SiO_2 wafer with 300 nm of dry oxide was used as a FET substrate. The latter substrate was rinsed in acetone and isopropanol before being exposed to oxygen plasma. A TI prime adhesion layer was spin-coated onto the substrate at 4000 rpm for 30 seconds then baked at 120°C for 2 minutes. AZ5214E photoresist was spin-coated onto the substrate at 4000 rpm for 30 seconds, followed by a baking step at 120°C for 90 seconds. Then, UV exposure with mask was conducted for patterning the photoresist, followed by a step of reversal bake at 126°C for 2 minutes and a flood exposure of 40 seconds. The resist was then developed using AZ726 and the substrate was rinsed with DI water. The electrodes were deposited by thermal evaporation of 5 nm Cr and 50 nm Au. Interdigitated electrodes with large spacing were also made using this procedure. In this case, the digits are 2.5 mm long, each digit is 10 μm wide and spaced from the next one by 10 μm.

Fabrication of Gold Nano-Stripes

250 nm PMMA was spin-coated and baked at 150°C for 15 minutes. To prevent charging effects, a layer of electra conductive resist was spin-coated on top of the PMMA layer. A

Raith eLine e-beam lithography system was employed for the exposure. The operating voltage was set at 20 kV and aperture was set at 10 μm. The dose was set to 160 μC/cm^2. The PMMA resist was developed in a solution of MIBK:IPA (1:3 in volume). The sample was cleaned again with oxygen plasma for 3 minutes before the deposition of 5 nm Cr and 50 nm Au by thermal evaporation. In this case, the digits are 200 μm long, each digit is 600 nm wide and spaced from the next one by 1 μm. An image of the electrode is given in Figure S20.

Film Deposition

All the deposition processes were performed in an oxygen and water-free glovebox. The original solution containing In_2S_3 nanocrystals was drop-casted onto the substrate (small drop of about 3 μL). The sample was then dipped in a solution of propylamine (1% vol) in ethanol for 4 minutes and subsequently rinsed in pure ethanol for at least 15 seconds to perform solid state ligand exchange. The sample was allowed to dry and the process was repeated a second time.

Transport Measurements

The sample was glued using a silver paste onto a substrate of sapphire covered with a gold layer and mounted on the cold finger of a cryostat. The gold layer was used as gate contact when transistor properties were studied. The transfer curves and the IV curves were measured using a Keithley 2634B SourceMeter which controls both the gate-source and the drain-source voltages, measuring the relative currents.

Assessment of the Gelling Power and Polarized-Light Microscopy

Dispersions of In_2S_3 nanoparticles in various organic solvents at different concentrations were filled into 2 mL glass vials and placed upside-down to assess their gel properties, and photographed with an Olympus XZ-1 digital camera.

Samples of dispersions were also filled into optical flat glass capillaries (Vitrocom, NJ, USA) of 100 μm thickness and 200 μm width to examine their textures with a polarizing microscope (Olympus BX51). When necessary, a wave-plate was inserted to determine the direction of the slow axis of well-defined birefringent domains. The optical textures were recorded with a sCMEX-20 camera (Euromex, Netherlands).

Results and discussion

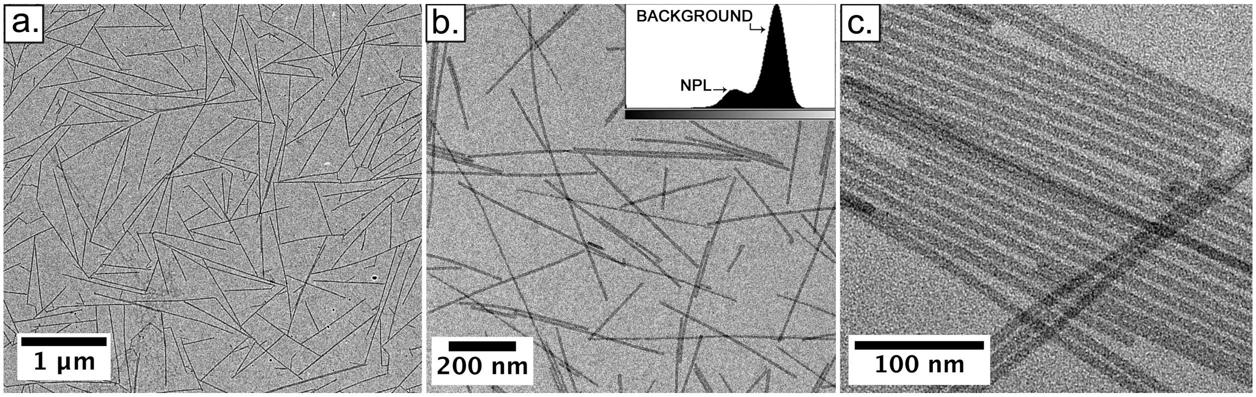

Figure 1: TEM images at different magnifications of In_2S_3 NR lying flat. The inset in (b) is a grey-scale histogram of the underlying image, showing the uniform thickness of the NR as only two peaks are seen (background and NR).

Indium sulfide nanoribbons (NR) are synthesized from molecular precursors by a fast and simple solvothermal method. Briefly, anhydrous indium (III) chloride is mixed with sulfur powder, water, and oleylamine in a Teflon-lined autoclave (see Figure S1 and experimental section for more details). The autoclave is then sealed and heated for two hours at 215°C in an oven. The resulting yellow viscous product is then washed with ethanol and toluene. Transmission Electron Microscopy (TEM) images of the resulting product show highly anisotropic nanoparticles with an average length of (1162 ± 44) nm and an average width of (8.7 ± 0.1) nm, as measured for an ensemble of 500 particles (see Figure 1, Figure S2, and SI for uncertainty calculations). The bimodal gray level distribution (inset of Figure

1b) indicates a homogeneous contrast between the particles lying flat and the TEM grid. This shows that the NR are flat objects with a well-defined thickness. Indeed, atomic resolution STEM examination of NR lying on their side (Figure 3c) shows a unique thickness for all the NR (0.71 nm). This highlights a very large aspect ratio of 1000 and 10, respectively, between their length and their width compared to their thickness. Additionally, UV-visible spectroscopy of NR dispersed in THF display an absorption peak centered at 247 nm (mainly due to oleylamine surface ligands), with a broad absorption tail into the visible range (up to 550 nm, due to In_2S_3 nanomaterial, Figure S3).

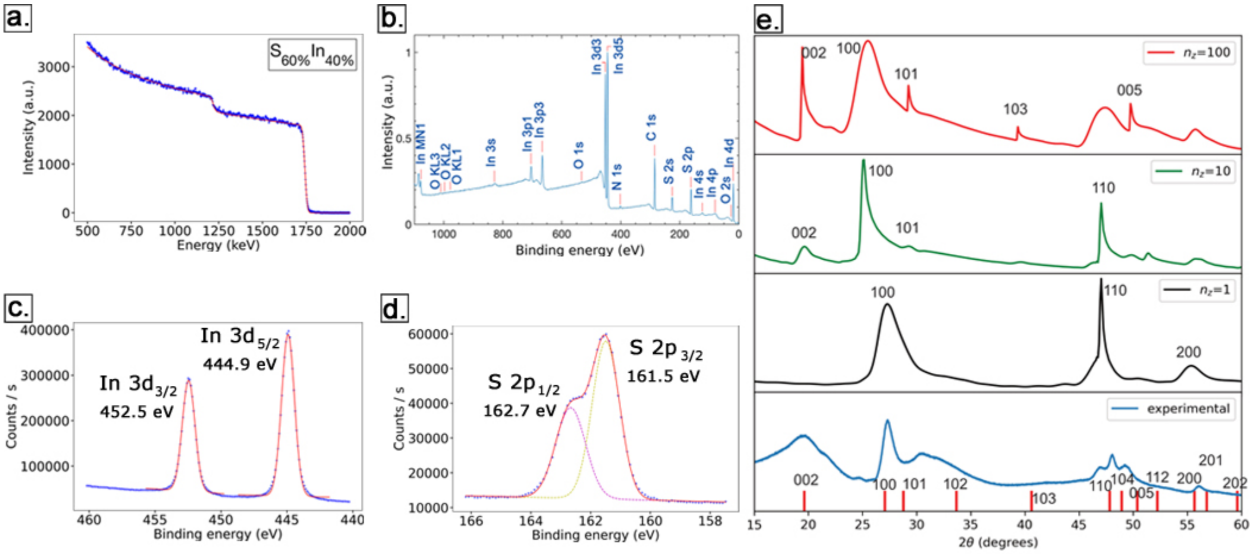

Figure 2: RBS, XPS and X-ray diffraction. (a) RBS spectrum for indium sulfide nanoribbons. The experimental data are fitted to obtain the chemical composition of the sample: 60% of sulfur and 40% of indium, yielding an In_2S_3 empirical formula. (b) Survey XPS spectrum. High-resolution XPS spectra of (c) In 3d and (d) S 2p. (e) X-ray diffraction of In_2S_3 NR. Experimental X-ray diffractogram for In_2S_3 NR (blue curve, bottom panel) overlaid with the theoretical bulk diffraction peaks of the γ-trigonal In_2S_3 (vertical red lines). Computed X-ray diffractograms (red, green, and black lines) for γ-In_2S_3 NR with a 1, 10, 100 aspect ratio in the three crystallographic orientations.

In order to identify the exact composition of the as-synthesized NR, we performed Rutherford Backscattering Spectrometry (RBS) experiments. This technique has already been used for CdSe nanoribbons[34] and is known to yield reliable and accurate results for the composition of inorganic materials, in particular for heavy elements. The powder material is irradiated by α-particles which are backscattered after interaction with the nuclei of the atoms composing the material. The energy of each backscattered ion is proportional to the initial energy of the α-particles by a factor k named kinematical factor, which depends on the atomic number of the chemical element. RBS analyses indicate that the NR are composed of (60 ± 1)% sulfur and (40 ± 1)% indium (Figure 2a). The stoichiometric ratio between indium and sulfur is thus 2:3, corresponding to an empirical formula In_2S_3. This composition is confirmed by Energy Dispersive X-Ray Spectroscopy analyses in the electron microcope where In and S mappings show the elemental disposition inside the NR (Figure S4).

To identify the NR crystalline structure, we performed X-Ray diffraction (XRD) experiments and compared the pattern with computed diffraction patterns of indium sulfide (Figures 2 and S6). Experimentally, we observe a broad peak at 19.5°, a low intensity peak at 24.6°, an intense narrow peak at 27.3° followed by two broader reflections at 30.5° and 31.8°. Finally, we observe a series of 3 peaks with one centered at 48° and two lower intensity peaks located at ± 1° (i.e. 47° and 49°) from the center peak. Low intensity peaks can be seen at 56.1°, 75.2° and 78.3°. Very similar diffraction patterns have been reported in several publications.[8,11,15,17,35–37] However, the indexation of the peaks varied in the different reports. The 27.3° peak has been attributed to the [311] reflection of the β phase in references[15,36–38] but to the [109] peak of the same phase in references[8,11] while other reports[17,35] assign this peak to the [110] reflection of the ϵ phase. These seemingly contradictory findings can be explained by the fact that the α cubic phase has been relabelled by some authors as the β phase because it appears at a higher temperature.[25] The peak at 19.5° has previously been attributed to impurities.[11] This is consistent with our observation of batch-to-batch variability in the relative intensity of this peak compared to the others. To check if this peak could be due to organometallic impurities, we acquired X-ray diffractograms for indium chloride, sulfur powder, a mixture of indium chloride in oleylamine and oleylamine alone. Since the broad peak at 19.5° is present for oleylamine alone (Figure S6), we thus concluded that this solvent is responsible for the presence of this peak.

Indexing the peaks and attributing the correct crystallographic structure can be made difficult in the case of nanostructures because the limited particle dimensions in some crystallographic directions induce a broadening of the diffraction peaks. To take this into account, we simulated the X-ray diffraction patterns of different atomic models of In_2S_3 NR whose dimensions match those observed using electron microscopy and we computed their diffraction patterns from the atomic positions using the Debye formula (Figure 2e) For the different allotropes, we changed the orientation of the edges with respect to the principal crystallographic axes to evaluate their influence on the X-ray diffractogram. The width of the peaks depends on the orientation of the crystalline lattice with respect to the edges. Let us consider a plate-like particle with dimensions 10×100×1 unit cells along the three a, b, c principal crystallographic axes. All the (hk0) reflections will be sharp since the crystallographic order along the a and b directions extends over a relatively long range. We also expect that the (0k0) reflections will be sharper than (h00) ones. Similarly, the (00l) reflections will be very broad or even undetectable since only one or a few unit cells are found along the c principal direction.[24]

We have simulated three different structures that are likely to match the experimental patterns: the α (Figure S7), β (Figure S8) and γ phases (Figure 2) with edge orientation along the principal crystallographic directions. For symmetry reasons, among six possibilities, only three yield a different diffraction pattern for the γ and β phases since the a and b axis are equivalent. Hence, only the number of unit cells along the c direction (n_z) influences the diffraction pattern. For the α phase, all three axes being equivalent, the orientation of the NR edge does not influence the diffraction pattern. Comparison of the computed α diffraction pattern to the experimental one shows that two predicted salient features are missing: the sharp [400] reflection (32°) and the [511] peak (43°). The same holds true for the β phase for which several peaks in the range of 40°-45° are visible in all computed patterns but are absent in our experimental data. In contrast, the computed diffractograms of the γ phase do not display sharp intense peaks that are not visible experimentally, with the exception of the [002] in the case of n_z=100 at around 20°. The experimental 27.3° and 48° reflections are well reproduced by theory for all the different orientations of the γ phase but our model does not predict the two broader reflections at 30.5° and 31.8° and the three peaks centered at 48°.

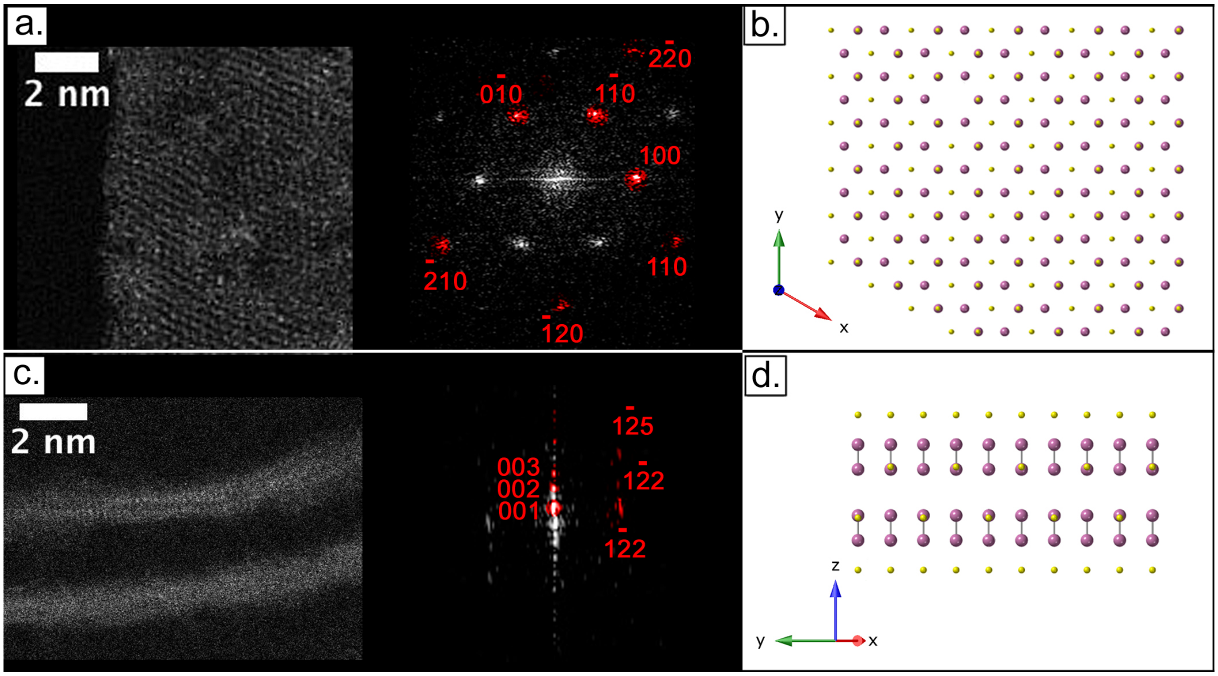

Figure 3: (a) HAADF-STEM image of In_2S_3 NR lying flat and its Fourier transform. Attributions are made with respect to γ-In_2S_3 structure. (b) Crystallographic γ-In_2S_3 model viewed along the normal to the (001) plane. (c) HAADF-STEM image of In_2S_3 NR lying on edge and its Fourier transform. Attributions are made with respect to γ-In_2S_3 structure. (d) Crystallographic γ-In_2S_3 model viewed along the normal to the (100) plane.
Atomic models of γ-In_2S_3 NR have a single conventional unit-cell thickness along the c-axis. Fourier transforms of TEM images match computed electron diffractograms of γ-In_2S_3.

In order to determine unambiguously the crystalline structure of the NR, we performed high-resolution electron microscopy experiments which show the presence of a ternary symmetry axis in the direction parallel to the thickness (Figure 3a), suggesting the γ phase which contains this element of symmetry. We thus compared this crystallographic model and experimental observations from HAADF-STEM images (Figure 3). Let us first consider NR lying flat on TEM grids (Figures 3a and b). Atoms are aligned in rows oriented at (58 ± 3)° (averaged from 55 measurements) from the edge of the particle. Within this row, atoms are separated by (0.39 ± 0.01) nm (averaged from 155 measurements) whereas two atoms vertically aligned (from different rows) are separated by (0.40 ± 0.01) nm (averaged from 174 measurements). Computed distances on modeled γ-In_2S_3 NR viewed along the normal vector of their (001) plane (i.e. simulation of a NR viewed lying flat, with its thickness along the c axis) are in good agreement with these experimental observations: atoms are aligned in rows oriented at 60° with respect to the edges, whereas in-row atoms and vertically-aligned atoms are 0.38 nm apart. Fast Fourier transforms (FFT) from In_2S_3 NR HAADF-STEM images match with modeled electron diffraction patterns of γ-In_2S_3 (Figure 3a and 3c). Indeed, 6-fold symmetry is observed in the FFT of HAADF-STEM images of In_2S_3 NR lying flat on the grid, and d-spacing measurements match those of the modeled electron diffractogram of γ-In_2S_3 viewed along the [001] direction (d=0.33 nm for the first ring spots, d=0.19 nm for the second ring spots). Additional NR HAADF-STEM images and the γ-In_2S_3 conventional-cell crystallographic representation are available in Figure S9. All this confirms our hypothesis that the In_2S_3 NR are in the γ phase, with their thickness along the c-direction. HAADF-STEM images of In_2S_3 NR lying on their edge show an atomically bilayered thickness, that is also well reflected in our crystallographic model (Figure 3c and d). The experimental thickness of this double layer ((0.71 ± 0.04) nm, averaged from 30 measurements) is close to the one given in our model (Figure 3d, 0.64 nm). Raman spectroscopy also points towards the γ-In_2S_3 structure. Indeed, the Raman spectrum (Figure S5) displays three broad peaks at 125 cm^{-1}, 193 cm^{-1} and 296 cm^{-1} which are compatible with the 9 Raman vibration active modes (combinations of $3A_{1g}$ + 3Eg) from the D_{3d} symmetry point group to which the γ phase is associated. Moreover, this Raman signature is very different from the ones of the α and β phases reported before in the literature,[27,39] strengthening its attribution to the γ phase. We stress that although multiple experimental observations (X-ray diffraction, electron microscopy and Raman spectroscopy) strongly suggest this attribution, our basic modeling of the X-ray diffractogram does not explain some experimental features such as the broad peaks found between 30° and 35° and the triple peak around 47°. We hypothesize that this could be due to ligand-induced strain affecting the nanostructure, which is not taken into account in our modeling.

Further insight into the chemistry of the NR is provided by X-Ray Photoelectron Spectroscopy (XPS) (Figure 2b-d). The interpretation of the survey spectrum gives the following atomic composition: C (65.9%), O (0.5%), S (18.6%), In (12.2%) and N (2.8%). The two peaks at 444.9 eV and 452.5 eV can be attributed to bonding energies of In $3d_{5/2}$ and In $3d_{3/2}$ (Figure 2c), while the two intense peaks at 161.5 eV and 162.7 eV correspond to the binding energies of $S2p_{3/2}$ and $S2p_{1/2}$, respectively (Figure 2d). These values indicate a sulfur form for both atoms (confirming an indium sulfide material) and are consistent with the reported values for In_2S_3.[15,40,41] Moreover, according to the peak areas of In $3d_{5/2}$ and S 2p, the In to S atomic ratio is 1.52, thus confirming the empirical formula of In_2S_3 obtained from RBS analysis. Additionally, the O 1s peak of the oxygen is centered around 531.7 eV which corresponds to C-O bonds, proving it is only related to ethanol molecules that may remain physisorbed on the surface of the NR during the different purification steps (Figure S10a). The N1s peak shows that nitrogen is either in an organic (24%) or ammonium (76%) form (Figure S10b). As nitrogen comes only from the oleylamine surface ligands ((2.3 ± 0.8) molecules.nm^{-2}), its content yields the following formula: $\{In_2S_3[\text{oleylamine/oleylammonium}]_{0.46}\}$ (see SI for calculation details). The NR coverage in amine is analogous to coverages reported, for instance, on wurtzite $\{CdSe[\text{n-octylamine}]_{0.53}\}$ quantum belts.[42,43]

We have probed the electronic conduction of an array of NR bundles. To make the film conductive, we have performed a solid-state ligand exchange during which the drop-casted film of NR is dipped in a dilute solution of propylamine in ethanol (1% in volume). When the film is deposited on interdigitated electrodes with large electrode spacing (10 μm > the NR length), we obtain a low level of current (sub nA) as shown in Figure 4. To increase the conductance of the film, we modified the device geometry to shrink the electrode spacing down to 1 μm, i.e. on the order of the NR length (Figure S20). In this case, we observed

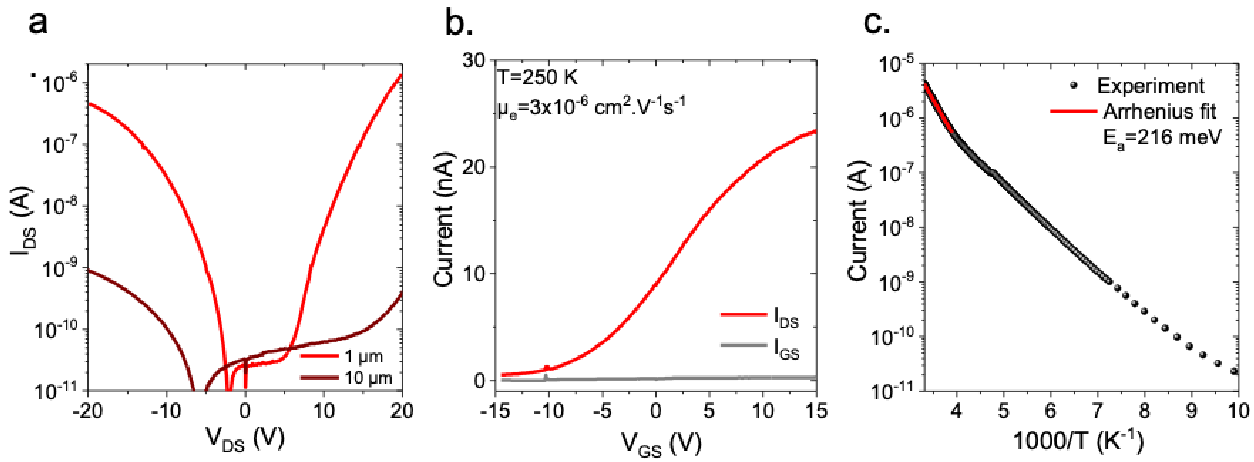

Figure 4: Transport properties of In_2S_3 nanoribbons. (a) I-V curves recorded at room temperature using 10 and 1 μm spaced interdigitated electrodes. (b) Transfer curves (drain and gate current as a function of applied under constant 5 V drain source bias), measured at 250 K using 1 μm spaced electrode. (c) Current as a function of temperature for the 1 μm spaced electrodes under 20 V drain source bias.

a large increase in the current magnitude, now reaching 1 μA. This drastic change of the conduction corresponds to a reduction of the material resistivity by a factor of 4000 and is consistent with the picture of hopping conduction for which the bottleneck remains the interparticle conduction. In this short electrode spacing geometry, we have been able to observe gate effect consistent with a n-type unipolar behavior (i.e. rise of conduction upon positive gate bias), as shown in Figure 4b. The film mobility remains low (μ_e=3×10^{-6} cm^2.V^{-1}s^{-1}), we can thus exclude a ballistic transport along the wire. Upon cooling (Figure 4c), the sample resistance increases. By fitting the current as a function of temperature with an Arrhenius law we can extract an activation energy of $\simeq$ 210 meV. Such a value, far below the half band gap ($E_G/2$=1.7 eV) value expected for an intrinsic semiconductor, suggests that shallow trap states near the conduction band actually drive the conduction.

We now focus on the experimental conditions of the synthesis. First, temperature and reaction time can be used to control the aspect ratio and length of the nanoribbons. Increasing one of these parameters yields an increase in the length, width and number of NR. For the same reaction time (15 minutes), an increase in the reaction temperature leads to

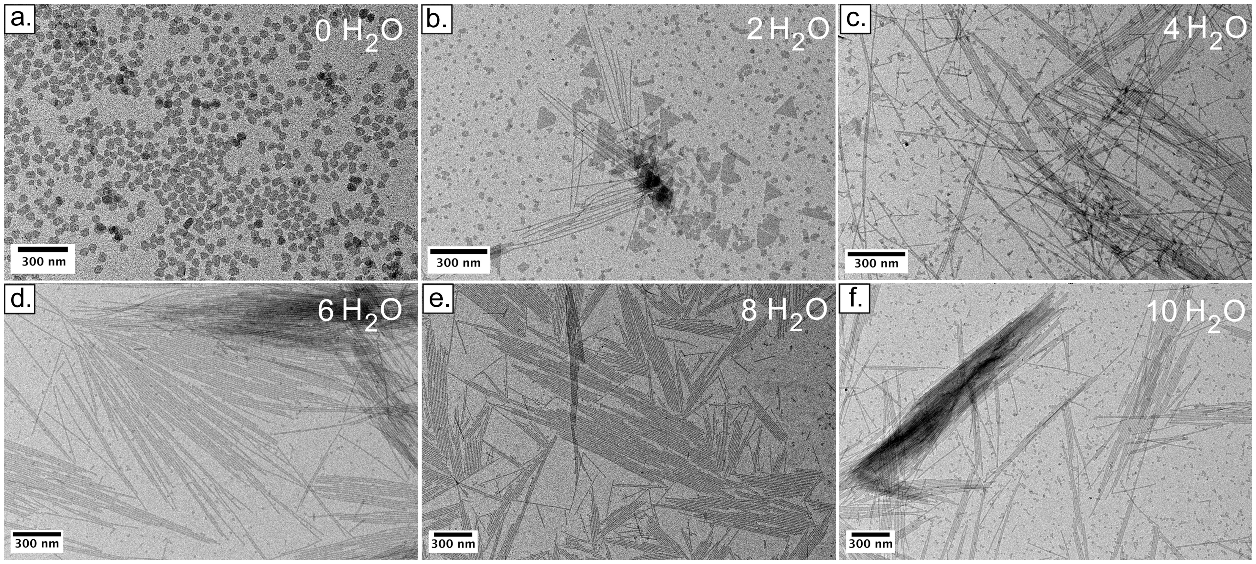

Figure 5: TEM images of products of syntheses where only the amount of water is varied with respect to the amount of indium chloride (in equivalents).

an increase in these features. Indeed, whereas no NR are produced at 180°C, NR with a length reaching up to 4 micrometers are obtained at 250°C (See Figure S11 and Table S0). Increasing the temperature speeds the reaction kinetics and favor longer and wider NR. The same trend is observed when the reaction time is increased at a given temperature (230°C). Indeed, after 15 minutes of reaction, NR are (238 ± 20) nm long and (6.0 ± 0.3) nm wide. After 2 hours of reaction, NR are (1.1 ± 0.2) μm long and (6.3 ± 0.3) nm wide. Increasing by a factor of 8 the reaction time leads to five times longer NR with the same width. This highlights the highly anisotropic character of the NR growth along their main axis. In any case, γ-In_2S_3 crystallographic phase is always obtained, independently of the reaction time or temperature and as shown in the X-Ray diffractograms on Figure S12.

We also found that traces of water in the synthesis had a critical effect on the shape of the resulting nanoparticle. By using an aged batch of indium chloride that had taken up water during storage, we found that the amount of water in the synthesis determines the shape of the final nano-objects. When a minimum of 8 equivalents of water with respect to indium chloride are added, long ultrathin In_2S_3 nanoribbons, as previously described, are obtained. In contrast, when indium chloride is anhydrous, hexagonal nanoplatelets are obtained (Figures 5a., S9 and S12). They are regular, with an average apothem of (26.9 ± 0.5) nm (measured on 200 nanoparticles), although some are elongated along one direction (Figure S13). Hexagonal nanoplatelets have the same composition as nanoribbons, as RBS measurements give a composition of the hexagons of (57 ± 1)% of sulfur and (43 ± 1)% of indium, consistent with EDX measurements (Figure S4). The small excess of indium might reveal the presence of unreacted indium chloride from the reaction along In_2S_3 NR. To further understand the evolution of shape from hexagons to nanoribbons, we realized a series of syntheses varying the amount of water in the initial mixture. For one equivalent of anhydrous indium (III) chloride, we added 0, 2, 4, 6, 8, or 10 equivalents of water. TEM images of the products of each synthesis are shown in Figure 5 and exhibit various nano-objects with shapes dependent on the amount of water added. Upon increasing water amount, the hexagons become smaller (up to twice smaller, with an average apothem of (14 ± 1) nm for 2 water equivalents added), before they completely disappear when 4 or more equivalents of water are added. NR with triangular shapes appear alongside hexagons for 2 to 6 equivalents of water (Figure 5b). The size of these equilateral triangles also decreases with increasing water amount, from an average size of (95 ± 3) nm to (16.8 ± 0.8) nm. As soon as 2 equivalents of water or more are present in the initial mixture, long nanoribbons appear and form bundles. The TEM images clearly show that the number of long NR increases with the amount of water in the medium. This correlates with the crude solution becoming gradually more and more viscous as the water content increases. The NR length reaches a maximum for 4 equivalents of water added (average length of (1.2 ± 0.1) μm and average width of (7.3 ± 0.2) nm, Figure 5c). When we further increased the water content from 6 to 10 equivalents, we observed dispersions of pure NR with lengths on the same order of magnitude. For all cases, similar X-Ray diffractograms are obtained (Figure S12), proving all objects have the crystallographic structure of γ- In_2S_3.

To understand the role of water on the formation mechanism we tested the addition of water during the synthesis (Figure S14 and S15). We start the synthesis without water, stop the heating after 2 hours and add 8 equivalents of water to the reaction medium before resuming the heating for 2 additional hours. After the initial 2 hours of heating, we observe hexagons with a mean edge length of 23 nm. When no water is added there is almost no effect of further heating on the final structure and we observed hexagons with the same, along with a few large triangles and NR (Figure S14). In contrast, when water is added, the prolonged heating leads to the formation of ribbons and large triangular nanoplatelets with edges of ca 227 nm that are much more numerous than in the anhydrous case. Prolonged heating for 20h in strictly anhydrous conditions (i.e. when the autoclave is sealed in a glovebox and without any intentional addition of liquid water) yields a mixture of NR with large lateral dimensions and nanosheets which roll up on themselves into tubular structures (Figure S15). Interestingly, these large sheets appear to result from the attachment and merging of smaller triangular nanoplates. When the same reaction is performed in air (i.e. with trace amounts of water in the reacting medium coming from ambient air) bundles of NR with lengths reaching several microns are obtained (Figure S16).

All these results show that water is a strong shape-directing agent as it triggers anisotropic growth from hexagons to long 1D ribbons. Without water, growth is isotropic but even traces of water induce the formation of ribbons. We can therefore tune the aspect ratio of colloidal In_2S_3 nanoribbons from 1 to more than 1000 just by adjusting the water content of the reacting medium. Although elucidating the atomic mechanism leading to this water-induced anisotropic growth will need further inquiry, previous reports have shown a strong effect of water on the synthesis of other materials. In the case of 2D ultrathin nanoplatelets, trace amounts of water have also been shown to have a dramatic effect on the morphology of Gd_2O_3 nanoplatelets whose structure changes from helices to triangular nanoplates when the amount of water is increased.[44] Bertrand *et al.*[45] have shown that water tunes the lateral aspect ratio for CdSe NR but in a trend opposite to ours since, in their study, increasing the water content decreases the aspect ratio. Water also inhibits the growth of InP quantum dots.[46] In this case, water is thought to be a source of hydroxide ions which are known to bind strongly on semiconducting nanoparticle surfaces.[47] Hydroxide adsorption on selected facets could slow down or enhance growth in a given direction and thus explain the increase of the particle aspect ratio when water is present. In our case, the basic nature of the reacting medium where an excess of amine is present will indeed favor the formation of hydroxide from water. Shape tuning caused by water thus seems to hold beyond the case of In_2S_3 nanoribbons. In order to prove further the generality of this phenomenon, we investigated the effect of water addition for another indium sulfide nanoplatelet synthesis which uses indium acetate as a precursor in an octylamine solvent[19] (see SI for experimental details). We have performed a series of experiments with varying amounts of water to assess its influence on the morphology of the final product. When anhydrous starting reagents are used and the synthesis is performed in a glovebox (i.e. under purely anhydrous conditions), we observed the formation of square nanoplatelets (Figure S17a). In contrast, even short contact with ambient atmospheric moisture induces the formation of curved nanoribbons (Figure S17b). This shape persists when larger amounts of water (between 1 and 10 equivalents with respect to indium) are added in a controlled fashion to the reaction media.

When redispersed after synthesis in toluene, the NR appear bundled, as shown in Figure 6a. Long aggregates of NR as large as 10 μm in length and 1 to 2 μm in width are observed in electron microscopy. These aggregates make the toluene dispersion hazy and sediment with time. The Small Angle X-ray Scattering (SAXS) patterns of NR dispersions in toluene (Figure 6c) display several sharp peaks which give information on the structure of the bundles. A first series of peaks at q^*, $2q^*$, and $3q^*$ where $q^* = 1.359$ nm^{-1}, related to a period $d^* = 2\pi/q^* = 4.62$ nm, is due to the lamellar stacking of the NR within the bundles. This stacking period is consistent with the length ($\ell \simeq 2$ nm) of two oleylamine molecules plus the thickness of the NR. Then, two broad peaks at smaller angles (0.41 nm^{-1} and 0.87 nm^{-1}), corresponding to periods of 15.4 nm and 7.2 nm, respectively, arise from some short-range

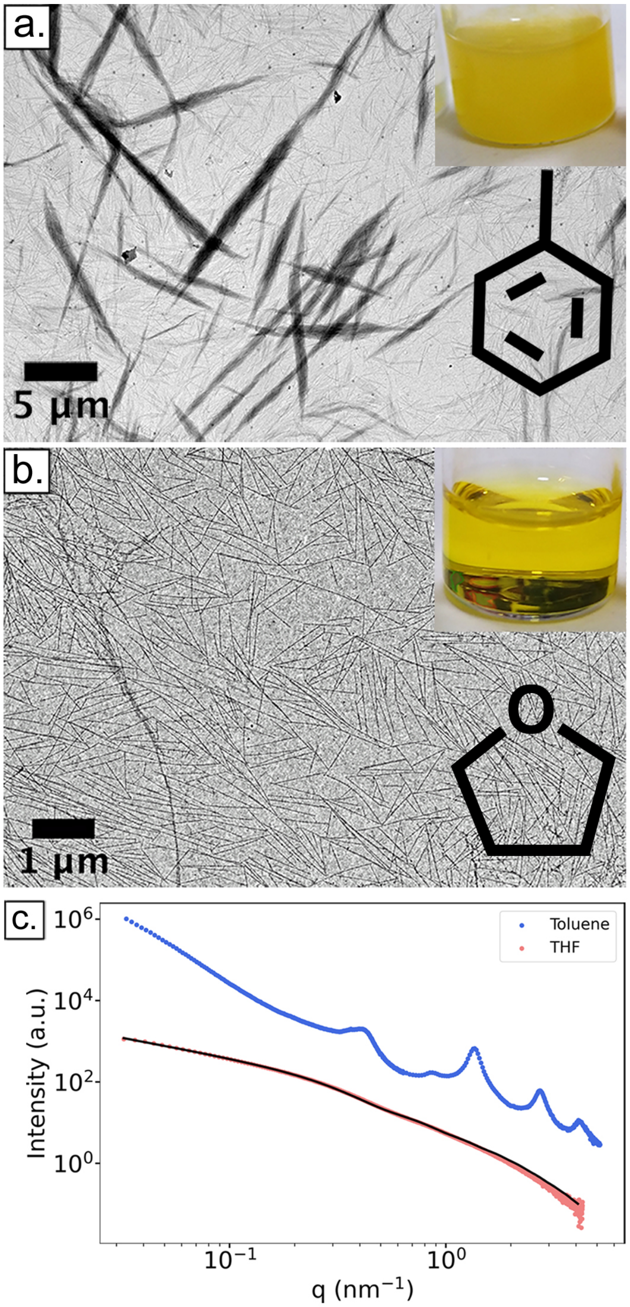

Figure 6: Bundling and unbundling of In_2S_3 NR dispersion, depending on the solvent for a concentration of 3.6 mg/mL. TEM images of the dispersion at the same NR concentration in (a) toluene and (b) THF. Insets are pictures of the colloidal dispersions. (c) SAXS patterns of a NR dispersion in a non-bundling solvent (THF, red symbols) and a bundling solvent (toluene, blue symbols). The former SAXS pattern is fitted to a model (black line) of polydisperse board-like parallelepipeds.

positional order within the plane of the NR. The corresponding distance is larger than w + 2 $\ell = 12.7$ nm where w is the width of the NR. Therefore, the NR are loosely packed in the direction parallel to their width within the bundles. When tetrahydrofuran is used instead of toluene, a clear and stable dispersion is readily obtained, indicating that the NR bundles do not form initially at this concentration (3.6 mg/mL) (Figure 6b). This is confirmed by the SAXS pattern shown in Figure 6c which does not display any peaks. Instead, the scattered intensity decreases regularly with increasing scattering angle, as expected for the form factor of isolated objects in solution. A fit of the SAXS pattern to a model of polydisperse board-like parallelepipeds (Figure 6c) displays excellent agreement with the data. The corresponding NR dimensions are 0.92 nm in thickness, 13.2 nm in width, and (1.2 ± 0.34) μm in length, which agrees with the TEM measurements.

Dispersions of In_2S_3 nanoribbons in various organic solvents such as tetrahydrofuran, chloroform, and cyclohexane form gels at very low concentrations (Figures 7a, b). With the density of bulk In_2S_3 of 4900 kg/m^3, the last gel sample in the dilution series of Figure 7b has a volume fraction of 0.07% and, occasionally, a sample of volume fraction of only ca 0.01% was also found to form a gel (Figure S18). Such gelation thresholds are much lower than those ($\simeq$ 1%) reported for other (hydrophilic) mineral systems such as swelling clay nanosheets, imogolite nanotubes, and V_2O_5 nanoribbons.[48–50] In fact, In_2S_3 nanoribbons have such a high gelling power in THF that they belong to the small class of so-called "supergelators" (i.e. below 0.1%) encountered with self-assembled fibrillar systems.[51–53] The low value of the percolating threshold in this system directly reflects the huge particle aspect ratio. Indeed, considering rod-like cylindrical particles, with L = 1 μm and effective diameter $D = (1 \times 10)^{1/2} \simeq 3$ nm, percolation is theoretically expected[54] at D/2L = 0.15%, in good agreement with our estimates. These values are also similar to those experimentally observed ($\simeq$0.2%) with single-wall carbon nanotubes, which is another case of extremely anisotropic nanoparticles.[55] Observations by polarized-light microscopy of concentrated (20.5 g/L) gels

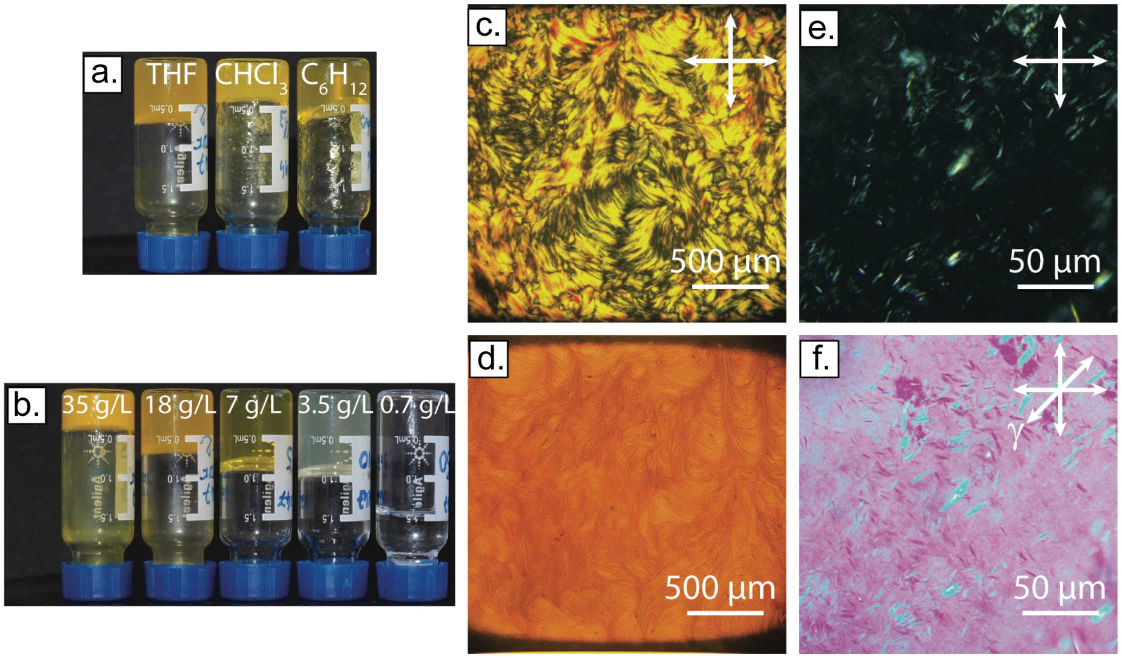

Figure 7: Gelation and birefringence properties of In_2S_3 nanoribbons. (a) Dispersions of In_2S_3 particles in tetrahydrofuran, chloroform, and cyclohexane form gels. (b) Series of vials filled with dispersions of In_2S_3 nanoribbons in THF at decreasing concentrations from left to right. The first four samples are gels whereas the last one is a sol. (c) Birefringent texture of a dispersion of In_2S_3 nanoribbons in THF at 20.5 g/L placed between crossed polarizers. (d) Image of the same sample observed in natural light (i.e. both the polarizer and analyzer have been removed). (e) High-magnification image of the same sample, recorded at the gel/solvent interface, showing small spindle-like birefringent objects. (f) Image of the same area observed after insertion of a wave-plate of slow axis denoted γ. In images (c), (e), and (f), the perpendicular double-headed arrows represent the directions of the crossed polarizer and analyzer.

in THF reveal a birefringent texture (Figure 7c) that is highly reminiscent of the threaded texture of nematic lyotropic liquid-crystals.[56] However, no clear isotropic/nematic biphasic domain could be detected, which is probably due to gelation. Observations of the same samples in natural light (Figure 7d) show a strong density contrast, which is usually not observed with nematic samples. This is most probably due to the existence at high concentration of a network of fibrils made of stacked In_2S_3 nanoribbons, reminiscent of the previously described NR bundling in toluene (Figure 6). Moreover, taking advantage of the gel syneresis that occurred over 1-2 years, we investigated the gel/solvent interface by optical microscopy and detected there the presence of small, Brownian, wispy birefringent objects (Figure 7e). These objects likely represent a first nanoribbon-stacking stage leading eventually to the large fibrillar objects that form the threaded texture (Figure 7c). Upon insertion of a wave-plate in the microscope optical path, the wispy objects that have their main axis parallel (resp. perpendicular) to the slow axis, γ, of the wave-plate appear blue (resp. red-orange) on the pink background (Figure 7f). This means that the slow axis of these objects is their main axis. Because the birefringence of In_2S_3 nanoribbons is most probably dominated by their form-birefringence, which leads to their highest refractive index occuring along their length, we infer that each wispy object is made of stacked nanoribbons aligned along its main axis.

Finally, we studied the effect of ambient moisture on the kinetics of gelation. We noticed that when stored in a glovebox, NR dispersions do not gel even after a prolonged storage period. For example, we have kept dispersions for over 6 months under moisture-free conditions and they retained their fluid character. We thus hypothesized that ambient moisture could play a role in the gelation. To test this hypothesis, we prepared three identical NR dispersions and kept them in different conditions: one in a nitrogen glovebox (moisture free), one under a fume hood and one under a controlled atmosphere with 95% relative humidity (see SI for experimental details and Figure S19). We found that the sample stored in the glovebox remained fluid while the other two samples yielded gels after different periods of time (Figure S19). Gelation occured after 10 days in 95% relative humidity but was slower under ambient atmosphere for which the relative humidity was smaller. Thus, moisture plays a key role in the gelation kinetics of our NR. Interestingly, this has already been noted for CdSe nanorods for which the liquid-crystalline phase could only be obtained under strictly anhydrous conditions since high concentration dispersions yielded gels under ambient atmosphere.[57,58] Israelachvili's group studied the effect of water on the colloidal interaction between surfactant-coated nanoparticles in apolar solvent using a surface force apparatus.[59,60] They showed that even trace amounts of water can have a dramatic effect on these interactions. As water is introduced into the system, it has a strong tendency to penetrate into the monolayer headgroup region and form water bridges between particles which induce a long-range attractive force and a strong friction at shorter length scales. This is consistent with our observations. In a dry environment, the particles are kept separated by the repulsive force induced by the monolayer, while in humid conditions water induces irreversible attraction between the NR which ultimately causes gelation.

Conclusion

To summarize, we successfully synthesized and characterized, using a combination of different techniques, indium sulfide nanoribbons with aspect ratio reaching 1000 and $P\overline{3}m1$ trigonal structure (γ-In_2S_3 phase). These NR could serve as a starting point for further ion exchange with potential applications beyond toxic Cd and Pb based semiconductors. We show that water has a critical role in the anisotropic growth of NR. The indium salt precursors being highly hygroscopic, we underline here that adventitious addition of an uncontrolled amount of water in the reacting medium can strongly impact the lateral dimensions of the NR. Dispersions of In_2S_3 NR in organic solvents can form gels at very low volume fractions whose rheological properties are worth investigating further. We also found a critical role of water on the gelation kinetics of the dispersion.

Acknowledgement

We acknowledge SOLEIL for provision of synchrotron radiation facilities and we would like to thank Thomas Bizien for assistance in using beamline SWING. This article is part of a project that has received funding from the European Research Council (ERC CoG SENECA) under the European Union's Horizon 2020 research and innovation program (Grant agreement No. 865995) and was supported by the LABEX iMUST of the University of Lyon (ANR-10-LABX-0064), created within the program Investissements d'Avenir set up by the French government and managed by the French National Research Agency (ANR). This work benefited from the use of the SasView application, originally developed under NSF award DMR-0520547. SasView contains code developed with funding from the European Union's Horizon 2020 research and innovation program under the SINE2020 project, grant agreement No 654000. We thank Tung Huu Dang for the short spacing electrode fabrication. SERMA technologies is acknowledged for XPS measurements.

Supporting Information Available

Supporting Information: Uncertainty calculations, ligand surface density calculations, effect of temperature on nanoribbon shape and supplementary figures including electron microscopy images, X-ray diffraction experiments and simulations, UV VIS and Raman spectra, photographs of gelled samples.

References

(1) Lhuillier, E.; Pedetti, S.; Ithurria, S.; Nadal, B.; Heuclin, H.; Dubertret, B. Two-Dimensional Colloidal Metal Chalcogenides Semiconductors: Synthesis, Spectroscopy, and Applications. *Acc. Chem. Res.* **2015**, *48*, 22–30.

(2) Ithurria, S.; Dubertret, B. Quasi 2D colloidal CdSe platelets with thicknesses controlled at the atomic level. *J. Am. Chem. Soc.* **2008**, *130*, 16504–5.

(3) Ithurria, S.; Tessier, M. D.; Mahler, B.; Lobo, R. P. S. M.; Dubertret, B.; Efros, A. L. Colloidal nanoplatelets with two-dimensional electronic structure. *Nature Materials* **2011**, *10*, 936–41.

(4) Schliehe, C.; Juarez, B. H.; Pelletier, M.; Jander, S.; Greshnykh, D.; Nagel, M.; Meyer, A.; Foerster, S.; Kornowski, A.; Klinke, C.; Weller, H. Ultrathin PbS Sheets by Two-Dimensional Oriented Attachment. *Science* **2010**, *329*, 550–553.

(5) Barreau, N. Indium Sulfide and Relatives in the World of Photovoltaics. *Solar Energy* **2009**, *83*, 363–371.

(6) Turan, E.; Zor, M.; Kul, M.; Aybek, A.; Taskopru, T. α-In_2S_3 and β-In_2S_3 Phases Produced by SILAR Technique. *Philosophical Magazine* **2012**, *92*, 1716–1726.

(7) Dalas, E.; Sakkopoulos, S.; Vitoratos, E.; Maroulis, G.; Kobotiatis, L. Aqueous Precipitation and Electrical Properties of In_2S_3: Characterization of the In_2S_3/Polyaniline and In_2S_3/Polypyrrole Heterojunctions. *Journal of Materials Science* **1993**, *28*, 5456–5460.

(8) Park, K. H.; Jang, K.; Son, S. U. Synthesis, Optical Properties, and Self-Assembly of Ultrathin Hexagonal In_2S_3 Nanoplates. *Angewandte Chemie International Edition* **2006**, *45*, 4608–4612.

(9) Choe, S.-H.; Bang, T.-H.; Kim, N.-O.; Kim, H.-G.; Lee, C.-I.; Jin, M.-S.; Oh, S.-K.;

Kim, W.-T. Optical Properties of β-In_2S_3 and β-In_2S_3 :Co^{2+} Single Crystals. *Semiconductor Science and Technology* **2001**, *16*, 98–102.

(10) Gorai, S.; Guha, P.; Ganguli, D.; Chaudhuri, S. Chemical Synthesis of β-In_2S_3 Powder and Its Optical Characterization. *Materials Chemistry and Physics* **2003**, *82*, 974–979.

(11) Tang, J.; Konstantatos, G.; Hinds, S.; Myrskog, S.; Pattantyus-Abraham, A. G.; Clifford, J.; Sargent, E. H. Heavy-Metal-Free Solution-Processed Nanoparticle-Based Photodetectors: Doping of Intrinsic Vacancies Enables Engineering of Sensitivity and Speed. *ACS Nano* **2009**, *3*, 331–338.

(12) Acharya, S.; Dutta, M.; Sarkar, S.; Basak, D.; Chakraborty, S.; Pradhan, N. Synthesis of Micrometer Length Indium Sulfide Nanosheets and Study of Their Dopant Induced Photoresponse Properties. *Chemistry of Materials* **2012**, *24*, 1779–1785.

(13) Li, M.; Tu, X.; Su, Y.; Lu, J.; Hu, J.; Cai, B.; Zhou, Z.; Yang, Z.; Zhang, Y. Controlled Growth of Vertically Aligned Ultrathin In_2S_3 Nanosheet Arrays for Photoelectrochemical Water Splitting. *Nanoscale* **2018**, *10*, 1153–1161.

(14) Kim, Y. H.; Lee, J. H.; Shin, D.-W.; Park, S. M.; Moon, J. S.; Nam, J. G.; Yoo, J.-B. Synthesis of Shape-Controlled β-In_2S_3 Nanotubes through Oriented Attachment of Nanoparticles. *Chemical Communications* **2010**, *46*, 2292.

(15) Franzman, M. A.; Brutchey, R. L. Solution-Phase Synthesis of Well-Defined Indium Sulfide Nanorods. *Chemistry of Materials* **2009**, *21*, 1790–1792.

(16) Acharya, S.; Sarkar, S.; Pradhan, N. Subnanometer Thin Beta Indium Sulfide Nanosheets. *The Journal of Physical Chemistry Letters* **2012**, *3*, 3812–3817.

(17) Sarkar, S.; Leach, A. D. P.; Macdonald, J. E. Folded Nanosheets: A New Mechanism for Nanodisk Formation. *Chemistry of Materials* **2016**, *28*, 4324–4330.

(18) Ni, B.; Liu, H.; Wang, P.-p.; He, J.; Wang, X. General Synthesis of Inorganic Single-Walled Nanotubes. *Nature Communications* **2015**, *6*, 8756.

(19) Wang, P.-p.; Yang, Y.; Zhuang, J.; Wang, X. Self-Adjustable Crystalline Inorganic Nanocoils. *Journal of the American Chemical Society* **2013**, *135*, 6834–6837.

(20) Tian, Y.; Wang, L.; Tang, H.; Zhou, W. Ultrathin Two-Dimensional β-In_2S_3 Nanocrystals: Oriented-Attachment Growth Controlled by Metal Ions and Photoelectrochemical Properties. *Journal of Materials Chemistry A* **2015**, *3*, 11294–11301.

(21) Wang, H.-Y.; Li, X.-F.; Xu, L.; Li, X.-S.; Hu, Q.-K. Phase Transition and Physical Properties of InS. *Communications in Theoretical Physics* **2018**, *69*, 211.

(22) Datta, A.; Gorai, S.; Panda, S. K.; Chaudhuri, S. A Simple Route to the Synthesis of Crystalline InS Nanowires from Indium Foil. *Crystal Growth & Design* **2006**, *6*, 1010–1013.

(23) Gorai, S.; Datta, A.; Chaudhuri, S. Solvothermal Synthesis and Characterization of InS. *Materials Letters* **2005**, *59*, 3050–3053.

(24) Holder, C. F.; Schaak, R. E. Tutorial on Powder X-Ray Diffraction for Characterizing Nanoscale Materials. *ACS Nano* **2019**, *13*, 7359–7365.

(25) Pistor, P.; Merino Álvarez, J. M.; León, M.; di Michiel, M.; Schorr, S.; Klenk, R.; Lehmann, S. Structure Reinvestigation of α-, β- and γ-In_2S_3. *Acta Crystallographica Section B Structural Science, Crystal Engineering and Materials* **2016**, *72*, 410–415.

(26) Diehl, R.; Carpentier, C.-D.; Nitsche, R. The Crystal Structure of γ-In_2S_3 Stabilized by As or Sb. *Acta Crystallographica Section B: Structural Crystallography and Crystal Chemistry* **1976**, *32*, 1257–1260.

(27) Horani, F.; Lifshitz, E. Unraveling the Growth Mechanism Forming Stable γ-In_2S_3 and β-In_2S_3 Colloidal Nanoplatelets. *Chemistry of Materials* **2019**, *31*, 1784–1793.

(28) Zhang, J.; Ding, L.; Sun, W.; Bi, W.; Wu, Z.; Gao, F. γ-In_2S_3 nanosheets-composed flowerlike nanostructure doped by Al^{3+} ions with optimal electronic structure and decreased work function of γ-In_2S_3 for CO_2 electroreduction to formate. *Journal of Alloys and Compounds* **2021**, *889*, 161770.

(29) Range, K.-J.; Zabel, M. ε-In_2S_3, a High Pressure Modification with Corundum Type Structure. *Zeitschrift für Naturforschung B* **1978**, *33*, 463–464.

(30) Matter, F.; Luna, A. L.; Niederberger, M. From colloidal dispersions to aerogels: How to master nanoparticle gelation. *Nano Today* **2020**, *30*, 100827.

(31) Sherman, Z. M.; Green, A. M.; Howard, M. P.; Anslyn, E. V.; Truskett, T. M.; Milliron, D. J. Colloidal Nanocrystal Gels from Thermodynamic Principles. *Accounts of Chemical Research* **2021**, *54*, 798–807.

(32) Green, A. M.; Ofosu, C. K.; Kang, J.; Anslyn, E. V.; Truskett, T. M.; Milliron, D. J. Assembling Inorganic Nanocrystal Gels. *Nano Letters* **2022**, *22*, 1457–1466.

(33) Zaccarelli, E. Colloidal gels: equilibrium and non-equilibrium routes. *Journal of Physics: Condensed Matter* **2007**, *19*, 323101.

(34) Singh, S.; Tomar, R.; ten Brinck, S.; De Roo, J.; Geiregat, P.; Martins, J. C.; Infante, I.; Hens, Z. Colloidal CdSe Nanoplatelets, A Model for Surface Chemistry/Optoelectronic Property Relations in Semiconductor Nanocrystals. *Journal of the American Chemical Society* **2018**, *140*, 13292–13300.

(35) Ye, F.; Wang, C.; Du, G.; Chen, X.; Zhong, Y.; Jiang, J. Z. Large-Scale Synthesis of In_2S_3 Nanosheets and Their Rechargeable Lithium-Ion Battery. *Journal of Materials Chemistry* **2011**, *21*, 17063–17065.

(36) Xing, Y.; Zhang, H.; Song, S.; Feng, J.; Lei, Y.; Zhao, L.; Li, M. Hydrothermal Synthesis

and Photoluminescent Properties of Stacked Indium Sulfide Superstructures. *Chemical Communications* **2008**, 1476.

(37) Lutfi Abdelhady, A.; Ramasamy, K.; Malik, M. A.; O'Brien, P. Very Narrow In_2S_3 Nanorods and Nanowires from a Single Source Precursor. *Materials Letters* **2013**, *99*, 138–141.

(38) Du, W.; Zhu, J.; Li, S.; Qian, X. Ultrathin β-In_2S_3 Nanobelts: Shape-Controlled Synthesis and Optical and Photocatalytic Properties. *Crystal Growth & Design* **2008**, *8*, 2130–2136.

(39) Kambas, K.; Spyridelis, J.; Balkanski, M. Far Infrared and Raman Optical Study of α- and β-In_2S_3 Compounds. *Physica Status Solidi (b)* **1981**, *105*, 291–296.

(40) Chen, L.-Y.; Zhang, Z.-D.; Wang, W.-Z. Self-assembled porous 3D flowerlike β-In_2S_3 structures: synthesis, characterization, and optical properties. *The Journal of Physical Chemistry C* **2008**, *112*, 4117–4123.

(41) Huang, W.; Gan, L.; Yang, H.; Zhou, N.; Wang, R.; Wu, W.; Li, H.; Ma, Y.; Zeng, H.; Zhai, T. Controlled synthesis of ultrathin 2D β-In_2S_3 with broadband photoresponse by chemical vapor deposition. *Advanced Functional Materials* **2017**, *27*, 1702448.

(42) Zhou, Y.; Wang, F.; Buhro, W. E. Large Exciton Energy Shifts by Reversible Surface Exchange in 2D II–VI Nanocrystals. *Journal of the American Chemical Society* **2015**, *137*, 15198–15208.

(43) Zhou, Y.; Buhro, W. E. Reversible Exchange of L-Type and Bound-Ion-Pair X-Type Ligation on Cadmium Selenide Quantum Belts. *Journal of the American Chemical Society* **2017**, *139*, 12887–12890.

(44) Liu, Y.; Li, Y.; Jeong, S.; Wang, Y.; Chen, J.; Ye, X. Colloidal Synthesis of Nanohelices

via Bilayer Lattice Misfit. *Journal of the American Chemical Society* **2020**, *142*, 12777–12783.

(45) Bertrand, G. H. V.; Polovitsyn, A.; Christodoulou, S.; Khan, A. H.; Moreels, I. Shape Control of Zincblende CdSe Nanoplatelets. *Chemical Communications* **2016**, *52*, 11975–11978.

(46) Xie, L.; Harris, D. K.; Bawendi, M. G.; Jensen, K. F. Effect of Trace Water on the Growth of Indium Phosphide Quantum Dots. *Chemistry of Materials* **2015**, *27*, 5058–5063.

(47) Zherebetskyy, D.; Scheele, M.; Zhang, Y.; Bronstein, N.; Thompson, C.; Britt, D.; Salmeron, M.; Alivisatos, P.; Wang, L.-W. Hydroxylation of the Surface of PbS Nanocrystals Passivated with Oleic Acid. *Science* **2014**, *344*, 1380–1384.

(48) Paineau, E.; Antonova, K.; Baravian, C.; Bihannic, I.; Davidson, P.; Dozov, I.; Impéror-Clerc, M.; Levitz, P.; Madsen, A.; Meneau, F.; Michot, L. J. Liquid-Crystalline Nematic Phase in Aqueous Suspensions of a Disk-Shaped Natural Beidellite Clay. *The Journal of Physical Chemistry B* **2009**, *113*, 15858–15869.

(49) Paineau, E.; Krapf, M.-E. M.; Amara, M.-S.; Matskova, N. V.; Dozov, I.; Rouzière, S.; Thill, A.; Launois, P.; Davidson, P. A liquid-crystalline hexagonal columnar phase in highly-dilute suspensions of imogolite nanotubes. *Nature Communications* **2016**, *7*, 10271.

(50) Davidson, P. Vanadium pentoxide gels: From "chimie douce" to "matière molle". *Comptes Rendus Chimie* **2010**, *13*, 142–153.

(51) Krishnan, B. P.; Sureshan, K. M. A Library of Multipurpose Supramolecular Supergelators: Fabrication of Structured Silica, Porous Plastics, and Fluorescent Gels. *Chemistry - An Asian Journal* **2018**, *13*, 187–193.

(52) Žinic, M.; Vögtle, F.; Fages, F. *Low Molecular Mass Gelator*; Springer Berlin Heidelberg: Berlin, Heidelberg, 2005; Vol. 256; pp 39–76, Series Title: Topics in Current Chemistry.

(53) Weiss, R. G.; Terech, P. *Molecular Gels: Materials with self-assembled fibrillar networks*; Springer: Dordrecht, 2006.

(54) Balberg, I.; Anderson, C. H.; Alexander, S.; Wagner, N. Excluded volume and its relation to the onset of percolation. *Physical Review B* **1984**, *30*, 3933–3943.

(55) Du, F.; Scogna, R. C.; Zhou, W.; Brand, S.; Fischer, J. E.; Winey, K. I. Nanotube Networks in Polymer Nanocomposites: Rheology and Electrical Conductivity. *Macromolecules* **2004**, *37*, 9048–9055.

(56) Gennes, P. G. d. *The Physics of Liquid Crystals*, 2nd ed.; Clarendon Press: Oxford, 1995.

(57) Li, L.-s.; Walda, J.; Manna, L.; Alivisatos, A. P. Semiconductor Nanorod Liquid Crystals. *Nano Letters* **2002**, *2*, 557–560.

(58) Li, L.-s.; Marjanska, M.; Park, G. H. J.; Pines, A.; Alivisatos, A. P. Isotropic-liquid crystalline phase diagram of a CdSe nanorod solution. *The Journal of Chemical Physics* **2004**, *120*, 1149.

(59) Godfrey Alig, A. R.; Akbulut, M.; Golan, Y.; Israelachvili, J. Forces between Surfactant-Coated ZnS Nanoparticles in Dodecane: Effect of Water. *Advanced Functional Materials* **2006**, *16*, 2127–2134.

(60) Min, Y.; Akbulut, M.; Prud'homme, R. K.; Golan, Y.; Israelachvili, J. Frictional Properties of Surfactant-Coated Rod-Shaped Nanoparticles in Dry and Humid Dodecane. *J. Phys. Chem. B* **2008**, *112*, 14395–14401.

Graphical TOC Entry